INTERNATIONAL JOURNAL OF AUTOMOTIVE AND MECHANICAL ENGINEERING
ISSN: 2229-8649 e-ISSN: 2180-1606
VOLUME 23, ISSUE 1, 2026, 13307 - 13320
DOI: https://doi.org/10.15282/ijame.23.1.2026.11.1009

RESEARCH ARTICLE

Air-cooled thermal management of electric vehicle batteries: Insights from CFD simulations on enclosure geometry configurations

Nasrul Hadi Johari[1,2]*, Haziq Abdul Razak[1], Mohd Adnin Hamidi[1,2] and Kumaran Kadirgama[1]

[1]Faculty of Mechanical and Automotive Engineering Technology, Universiti Malaysia Pahang Al-Sultan Abdullah, 26600 Pekan, Pahang, Malaysia
[2]Centre for Advanced Industrial Technology, Universiti Malaysia Pahang Al-Sultan Abdullah, 26600 Pekan, Pahang, Malaysia

Abstract – In the rapidly advancing field of electric vehicles (EVs), optimizing battery thermal management is crucial for enhancing performance, safety, and lifespan. EV batteries are prone to overheating, which can significantly degrade their efficiency and longevity, posing safety risks. This study employs Computational Fluid Dynamics (CFD) simulations to evaluate six air-cooled battery thermal management system (BTMS) designs, including the high-performing BTMS-H and BTMS-J configurations. The analysis focuses on the effects of inlet air velocity and battery pack enclosure geometry on temperature distribution, airflow patterns, and pressure gradients. The methodology involved steady-state, incompressible simulations using ANSYS Fluent, with mesh construction, grid-independence testing, and validation against experimental data, yielding relative errors between 6.5% and 11.9%. Results indicate that higher inlet velocities significantly improve heat dissipation and temperature uniformity. BTMS-H and BTMS-J achieved the highest heat transfer coefficients (190.020 W/m²·K and 187.266 W/m²·K, respectively). In BTMS-H, increasing inlet velocity from 2 m/s to 4 m/s reduced the average temperature from 310.38 K to 307.75 K. Enlarging inlet/outlet sizes further decreased temperatures, demonstrating the importance of optimizing duct dimensions for improved airflow. These findings provide practical guidance for designing compact, energy-efficient, and thermally safe BTMS in EVs, thereby supporting the development of more reliable and high-performance electric vehicle battery systems.

Article History
Received : 04 February 2025
Revised : 15 July 2025
Accepted : 04 December 2025
Published : 12 March 2026

Keywords
BTMS
CFD
Electric vehicle
Battery performance
Cooling system

1. Introduction

Electric vehicles (EVs) play a pivotal role in the global transition to sustainable transportation [1]. This shift is propelled by governments' policies and industry initiatives aimed at reducing reliance on fossil fuels and mitigating greenhouse gas emissions [2, 3]. Since 2011, continuous initiatives within the European Union to champion green energy and reduce pollution from conventional internal combustion engine vehicles have significantly propelled electric vehicle adoption [4]. To achieve both an extended driving range and swift acceleration, electric vehicles require energy storage systems that are highly efficient and capable of delivering substantial power. Consequently, considerable research effort is focused on advancing lithium-ion battery technology. These batteries are widely employed in electric, hybrid electric, and plug-in hybrid electric vehicles, primarily owing to their high energy density, robust stability, and low self-discharge rates [5–7]. Nevertheless, their overall performance, critical cycle life, and intrinsic safety are all critically contingent upon effective thermal management strategies [8]. In parallel, internal combustion engines continue to pose serious environmental and public health concerns due to emissions of CO, CO_2, NOx, and particulate matter. Numerous strategies have been proposed to mitigate these emissions, including alternative fuels, engine modifications, and exhaust aftertreatment systems. Among alternative fuels, alcohol-based blends such as butanol and ethanol have shown measurable reductions in CO emissions, although trade-offs in NOx formation and combustion efficiency have been observed depending on engine load and speed conditions [9,10].

Nanomaterials offer a promising route to enhance both emission control and combustion efficiency. Recent advances in the use of carbon-based nanomaterials, particularly graphene nanoplatelets (GNPs), have drawn increasing attention due to their unique thermal and catalytic properties. Studies have shown that blending diesel with GNPs can improve brake thermal efficiency, torque, and power output while simultaneously reducing emissions under high-load conditions [11,12]. Furthermore, the thermal conductivity of GNPs positions them as promising materials not only for combustion efficiency in ICEs but also for potential thermal management applications in lithium-ion batteries—an emerging cross-domain research area with implications for both EVs and hybrid platforms [11]. Battery thermal management systems (BTMS) are designed to maintain lithium-ion batteries within an optimal operating temperature range (20–50 °C), ensuring safety, performance, and longevity [13,14]. Various BTMS technologies have been explored, including air cooling [15,16], liquid cooling [17,18], phase change materials [19,20], and heat pipes [21,22]. Among these, air cooling remains attractive due to its simplicity, cost-effectiveness, and ease of integration into vehicle architectures [23,24]. However, its lower heat removal capacity compared to liquid-based systems can result in higher temperature gradients, particularly under high load conditions [25,26]. Elevated temperatures accelerate battery degradation by reducing capacity, increasing internal resistance, and raising the risk of thermal runaway [27-29]. Air-cooled BTMS—typically using either passive natural convection or active forced convection—face challenges in achieving uniform temperature distribution across all cells in a pack, leading to thermal imbalances that degrade performance [13,14], [25].

*CORRESPONDING AUTHOR | Nasrul Hadi Johari | ✉ nhadi@umpsa.edu.my

Prior studies have attempted to enhance air-cooled BTMS performance through geometry optimization and airflow control strategies. For instance, Pan et al. [30] incorporated a fan at the base of a Z-type enclosure, reducing both peak temperature and temperature differentials. Lan et al. [31] introduced reverse-layered airflow with optimized inlet and outlet deflector angles, achieving a 36.4% reduction in temperature differences. Zhang et al. [32] adjusted parallel channel widths and duct geometries, leading to significant improvements in cooling uniformity, while a subsequent study [33] optimized parallel channel widths to achieve over a 72% reduction in temperature differentials. In terms of control strategies, He et al. [34] optimized airflow in a sequential cooling system based on the location of the maximum temperature, reducing power consumption by 84%. Wang et al. [35] developed a reciprocating airflow method that maintained a maximum temperature difference of 4.9°C, while Liu et al. [36] switched between J-, U-, and Z-type flow patterns to limit temperature differences to 1.33 K. Chen et al. [23,24] applied dynamic airflow adjustments in J-type systems, reducing cell temperature differentials by more than 67%. While these studies highlight valuable advances, most focus on a single aspect of BTMS design and do not directly compare multiple enclosure geometries and airflow configurations under consistent evaluation criteria. This limits the ability to generalize findings or identify the most effective design parameters across different scenarios. Despite these advances, most prior research has examined isolated design aspects without a systematic comparison across multiple battery enclosure geometries and airflow configurations. Consequently, there is a lack of comprehensive understanding of how these parameters jointly influence temperature uniformity, cooling performance, and energy efficiency. The objective of this study is to numerically investigate the performance of air-cooled BTMS across different battery enclosure geometries, considering variations in airflow velocity and spatial configuration. By systematically comparing configurations, this work aims to identify optimal design parameters that improve cooling effectiveness and energy efficiency, thereby enhancing the safety and reliability of air-cooled BTMS in EV applications.

2. Materials and Methods

A comprehensive CFD analysis was conducted to evaluate the thermal performance of six distinct air-cooled BTMS configurations. This methodology simulates airflow and temperature fields within the BTMS to assess the influence of critical design parameters, i.e., inlet velocity and enclosure geometry, on the thermal regulation of battery packs.

2.1 Computational Fluid Model

To evaluate the cooling efficacy of BTMS, it is crucial to obtain the flow field and temperature field of the system. CFD is an effective method for calculating the flow field of the system. This work utilizes the CFD approach to determine the average temperature, peak temperature, and maximum temperature differentials in the BTMS. BTMS. The Reynolds number for the incoming wind speed of the air-cooling BTMS typically exceeds 3000, indicating that the airflow within the BTMS is characterized by transitional and turbulent flows. The governing equations of the airflow are the Reynolds-averaged Navier-Stokes Equations (RANS) incorporating Menter's hybrid *k-ϵ/k-ω* Shear Stress Transport model with the transitional model (SST-Tran) [37,38] to disturbed flow features in the enclosure. As the cooling air was assumed steady and incompressible, the governing equations are listed below. The flow was assumed steady and incompressible, with density treated as constant throughout the domain. Incompressibility was enforced by solving the continuity equation under this constant-density assumption, while pressure–velocity coupling was employed to maintain a divergence-free velocity field. Under these conditions, the governing equations of mass, momentum, and energy conservation are expressed as follows:

1. Continuity Equation:

$$\frac{\partial u_i}{\partial x_i} = 0$$

2. Momentum Equation:

$$\frac{\partial (u_i u_j)}{\partial x_j} = -\frac{\partial p}{\partial x_i} + \frac{\partial}{\partial x_j}\left[\left(\mu + \frac{\mu_t}{\sigma_k}\right)\frac{\partial u_j}{\partial x_j}\right] \tag{2}$$

3. Turbulent Kinetic Energy (k) equation:

$$\frac{\partial (\rho u_i k)}{\partial x_i} = \frac{\partial}{\partial x_j}\left[\left(\mu + \frac{\mu_t}{\sigma_k}\right)\frac{\partial k}{\partial x_j}\right] + P_k - \beta^* \rho \omega k + \frac{\partial}{\partial x_j}\left[\left(\mu + \frac{\mu_t}{\sigma_k}\right)\frac{\partial u_i}{\partial x_j}\right] \tag{3}$$

Eq. (3) models the transport of turbulent kinetic energy k, representing the intensity of turbulence generated in the airflow within the BTMS enclosure. In this study, k quantifies how geometric features such as inlet duct shape or cell arrangement influence turbulence eddies, which directly affect convective heat transfer from battery surfaces.

4. Specific Rate of Dissipation (ω) equation:

$$\frac{\partial (\rho u_i \omega)}{\partial x_i} = \frac{\partial}{\partial x_j}\left[\left(\mu + \frac{\mu_t}{\sigma_\omega}\right)\frac{\partial \omega}{\partial x_j}\right] + \frac{\beta}{\rho} P_k - \beta^* \rho \omega^2 + 2(1 - F_1)\frac{\sigma_{\omega 2}}{\omega}\frac{\partial k}{\partial x_j}\frac{\partial \omega}{\partial x_j} + \frac{\partial}{\partial x_j}\left[\left(\mu + \frac{\mu_t}{\sigma_\omega}\right)\frac{\partial u_i}{\partial x_j}\right] \tag{4}$$

Eq. (4) determines the rate at which turbulence dissipates into thermal energy. For BTMS flows, ω helps capture near-wall effects inside narrow cooling channels, improving the prediction of local heat transfer rates on battery surfaces.

5. Intermittency (γ) Equation (Transitional Part):

$$\frac{\partial(\rho u_i \gamma)}{\partial x_i} = \frac{\partial}{\partial x_j}\left[\left(\mu + \frac{\mu_t}{\sigma_\gamma}\right)\frac{\partial \gamma}{\partial x_j}\right] + \beta^* \rho(1-\gamma)P_k - \beta^* \rho \omega \gamma + \frac{\partial}{\partial x_j}\left[\left(\mu + \frac{\mu_t}{\sigma_\gamma}\right)\frac{\partial u_i}{\partial x_j}\right] \quad (5)$$

The intermittency function γ governs the transition from laminar to turbulent flow. In BTMS applications, this is particularly important because airflow entering the battery enclosure may initially be laminar, with turbulence developing downstream due to geometry-induced disturbances such as bends, spacers, or deflectors.

6. For the specific dissipation rate (α) equation (Transitional Part):

$$\frac{\partial(\rho u_i \gamma)}{\partial x_i} = \frac{\partial}{\partial x_j}\left[\left(\mu + \frac{\mu_t}{\sigma_\alpha}\right)\frac{\partial \alpha}{\partial x_j}\right] + \beta \rho P_k - \beta \rho \omega \alpha + 2(1-F_1)\frac{\sigma_{\alpha 2}}{\alpha}\frac{\partial k}{\partial x_j}\frac{\partial \alpha}{\partial x_j} + \frac{\partial}{\partial x_j}\left[\left(\mu + \frac{\mu_t}{\sigma_\alpha}\right)\frac{\partial u_i}{\partial x_j}\right] \quad (6)$$

The variable α refines transitional flow predictions when used alongside γ, enhancing accuracy in modeling boundary-layer behavior. In the BTMS context, this improves predictions of heat transfer in regions where the airflow remains partly laminar, such as low-velocity zones behind battery modules. where u_i is the velocity components, p is the Reynolds-averaged pressure, and ρ and μ are the density and viscosity of the airflow, respectively. For the turbulent equations, μ_t represents the eddy viscosity, k is the turbulent kinetic energy, ω and α are the specific rates of dissipation. Meanwhile σ_k, σ_ω, β, β^*, F_1, and others are the model constants. SST-Tran variant is designed to handle both fully turbulent and transitional boundary layers and has proven in a wide range of engineering problems, including turbomachinery and aircraft configurations [38], and cardiovascular flow applications [39,40].

For the heat distribution in the battery pack, the temperature field evolves as the air flows, exchanges heat with the surrounding, i.e., battery cells and the enclosure wall. The general energy equation for the cooling air in steady-state conditions [41] is as follows.

$$u_i \frac{\partial T}{\partial x_i} = \frac{\partial}{\partial x_j}\left(k_T \frac{\partial T}{\partial x_j}\right) + Q \quad (7)$$

where T is the temperature, k_T is the thermal conductivity, and Q represents the volumetric heat generation rate from the battery cells (W/m³). This equation enables the coupling between the fluid's thermal field and the heat source from battery cells, thus providing insight into the BTMS's cooling effectiveness. In the CFD simulation, the energy equation was coupled with the fluid flow equations to comprehensively simulate heat transfer in a fluid domain.

2.2 Geometry of the BTMS

The air-cooling was modeled flowing into the battery pack enclosure of the BTMS in a steady state and incompressible conditions. To ensure the flow is uniform, the inlet length was extended to 5D long before reaching the battery cell, and the wall was assumed to have a no-slip condition. Two inlet/outlet heights, 20 mm and 40 mm, were selected to represent practical dimensional limits for EV battery module cooling ducts. The smaller dimension (20 mm) reflects space-constrained designs commonly used in compact enclosures, while the larger dimension (40 mm) represents an upper bound that can be implemented without major changes to the enclosure or vehicle architecture. The battery cell size is based on a 18650-type Lithium-ion cell measuring 19mm in diameter and 65 mm in length [42]. A total of 40 batteries were arranged according to an inline configuration. Considering different heat distribution patterns in the BTMS, this study delved into a comprehensive examination of six distinct BTMS types, aiming to study the heat distribution and airflow dynamics within the enclosures shown in Table 1. The BTMS geometries used in this study were adapted from previously published research that investigated cooling performance and associated energy consumption[23,41,43–45]. It is essential to note that these BTMS geometries have been scaled down from their original automotive applications, which typically involve a significantly larger number of battery cells, to suit the scope and objectives of the present study.

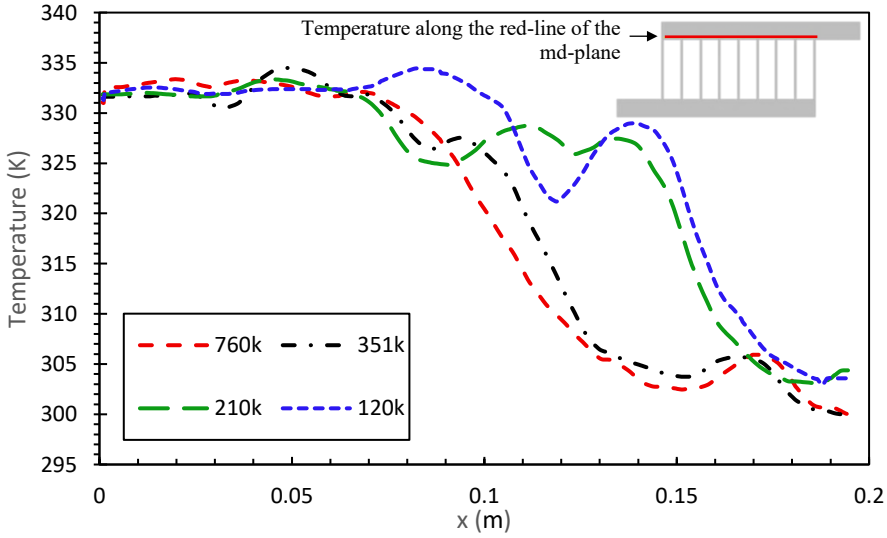

Figure 1. Mesh independence test using BTMS-Z model comparing different sets of meshes in measuring temperature along the model mid-plane

Table 1. Variations of BTMS enclosure designs used

No.	Enclosure	Geometry
1	**BTMS-Z** The inlet and outlet are oriented perpendicularly to the cooling channels and in opposing directions.	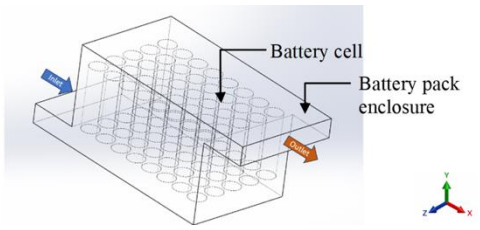
2	**BTMS-U** Inlet and outlet are perpendicular to the cooling channels and in the same direction.	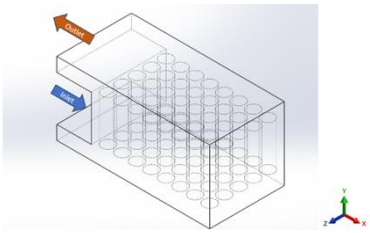
3	**BTMS-J** Combination of Z and BTMS-U to improve airflow with two outlets. Better temperature distribution.	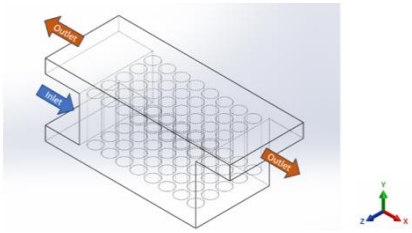
4	**BTMS-Z (Optimized)** The inlet side plenum is gradually decreased	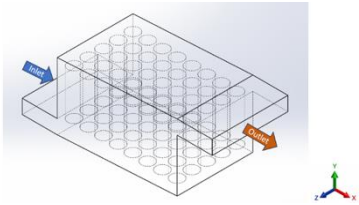
5	**BTMS-H** Based on BTMS-U, an additional inlet and outlet on the other side of the enclosure. Improved temperature distribution	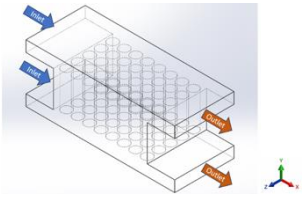
6	**BTMS-T** One inlet perpendicular to two outlets	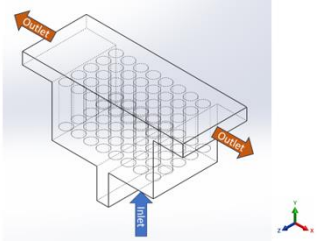

For the mesh models, three sets of mesh sizes representing normal, finer, and extremely fine were implemented for all BTMS designs to ensure a grid-independence solution. The meshes were carefully constructed using ANSYS FLUENT Meshing with more focus on the surfaces around the batteries and the gaps between the batteries. The mesh independence test was first carried out to ensure the simulation accuracy. A mesh independence test was performed with the BTMS-Z model (Figure 1). The maximum temperature difference along the battery midplane between the fine mesh (351,450 elements) and the extremely fine mesh (760,455 elements) was only 6%. Since this variation is within an acceptable tolerance, the fine mesh with 351,450 elements was selected for all subsequent simulations to balance accuracy and computational efficiency.

2.3 Boundary Conditions and Computational Details

Table 1 presents the design configurations of the air-cooled BTMS models, highlighting variations in inlet and outlet arrangements. The boundary conditions for the inlets were defined as velocity-inlet, while the outlets were set as pressure-

outlet conditions. A no-slip boundary condition was applied to the interior surfaces of the enclosure to account for realistic airflow behavior. The structural components, including the battery and enclosure walls, were modeled using aluminum material properties, as detailed in Table 2. The inlet air temperature was set to a room temperature of 300.15 K, and three different inlet velocities, i.e., 2 m/s, 3 m/s, and 4 m/s, were simulated under steady-state conditions across all BTMS configurations [40] [46]. At the outlet, a total static pressure of 1 atm was imposed at the inner surface of the enclosure exit. The external boundaries were treated as adiabatic to prevent heat exchange with the surroundings. For the battery, a uniform temperature of 318.15 K was set, considering its maximum temperature at a discharged rate of 3C under natural convection [31]. Coupled boundary conditions were used at the interfaces between the battery pack and the surrounding air to ensure accurate thermal interaction. The simulations were conducted using ANSYS FLUENT 2023. A second-order upwind scheme was employed to discretize the convective terms, while a central difference scheme was applied to the diffusive terms in the governing equations. The SIMPLE algorithm was used to solve the equations, with the residuals of the continuity, momentum, and energy equations set to a convergence criterion of 10^{-5} to ensure the precision of the numerical solution.

Table 2. Thermo-physical properties of air and the solid material

Material Type	Density (kg/m^3)	Thermal Conductivity (W/m.K)	Heat Capacity (J/kg.K)	Viscosity (Pa.s)
Air	1.225	0.0242	1006.43	1.7894e-05
Lithium-ion	2800	37.6	1200	-
Aluminum	3880	202.4	871	-

3. Results and Discussion

3.1 CFD Model Validation

Before conducting simulations for all enclosure types, confirming the model's accuracy is imperative to ensuring its concordance with a real-world experiment. Validation involves referencing an experimental study, in this case, the work conducted by Chen et al. [41], which employed a BTMS-Z enclosure to measure temperatures within the BTMS. The experimental setup included using aluminum blocks to mimic battery cells, each embedded with three heating rods powered by a DC supply. Thermocouples were strategically placed at the center of each aluminum block's surface. The simulation replicates the experiment, adhering to the specified properties and conditions. A plane was strategically selected from the model's midsection to mitigate temperature effects from enclosure walls. The simulations were executed at velocities of 3.5 and 4.0 m/s, and temperatures at two points were measured. Figure 2 illustrates the temperature distribution across the cross-section of the BTMS-Z model. A midsection plane was selected to capture temperature variations, as shown in Figure 3, which depicts the chosen plane and the corresponding simulation results. The comparative analysis indicates minimal discrepancies between the simulated and experimental outcomes. From Figure 4, the maximum absolute temperature difference between simulation and experiment was 0.8 K at an inlet velocity of 3.5 m/s and 0.4 K at 4.0 m/s, as detailed in Table 3. The corresponding relative errors in the predicted temperature differences were 11.9% for the 3.5 m/s case and 6.5% for the 4.0 m/s case, calculated using the formula (|Simulated – Experimental|/Experimental×100%). These low error margins demonstrate the strong correlation between the simulation and experimental results, reinforcing the accuracy of the computational model.

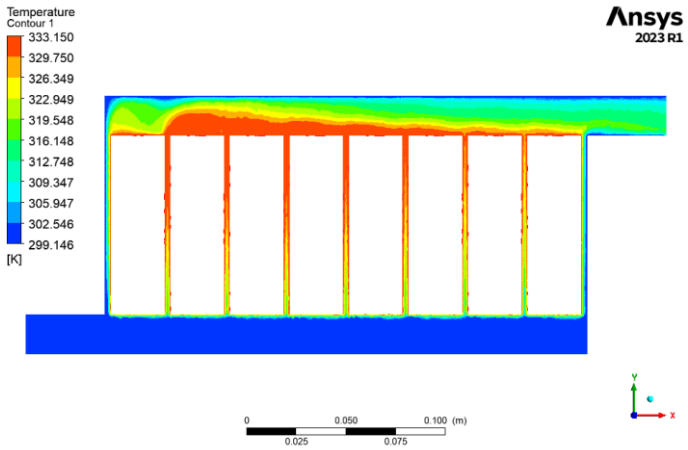

Figure 2. Temperature distribution contours on a mid-plane of BTMS-Z

Table 3. Temperature recorded at T2 and T3 on the midplane of BTMS-Z during inlet air velocities of 3.5 m/s and 4 m/s

Inlet velocity (m/s)		T2 (K)	T8(K)	T8-T2 (K)
3.5	Experiment [37]	328.2	321.5	6.7
	CFD	327.5	321.6	5.9
4.0	Experiment [37]	325.0	318.8	6.2
	CFD	324.5	318.7	5.8

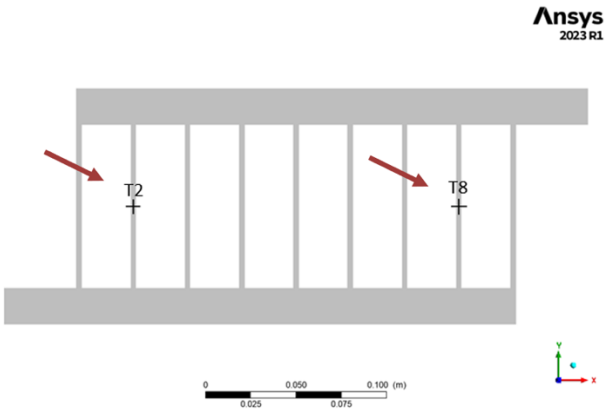

Figure 3. Location of T2 and T3 on the midplane of BTMS-Z used for temperature comparison between the experimental and simulation results

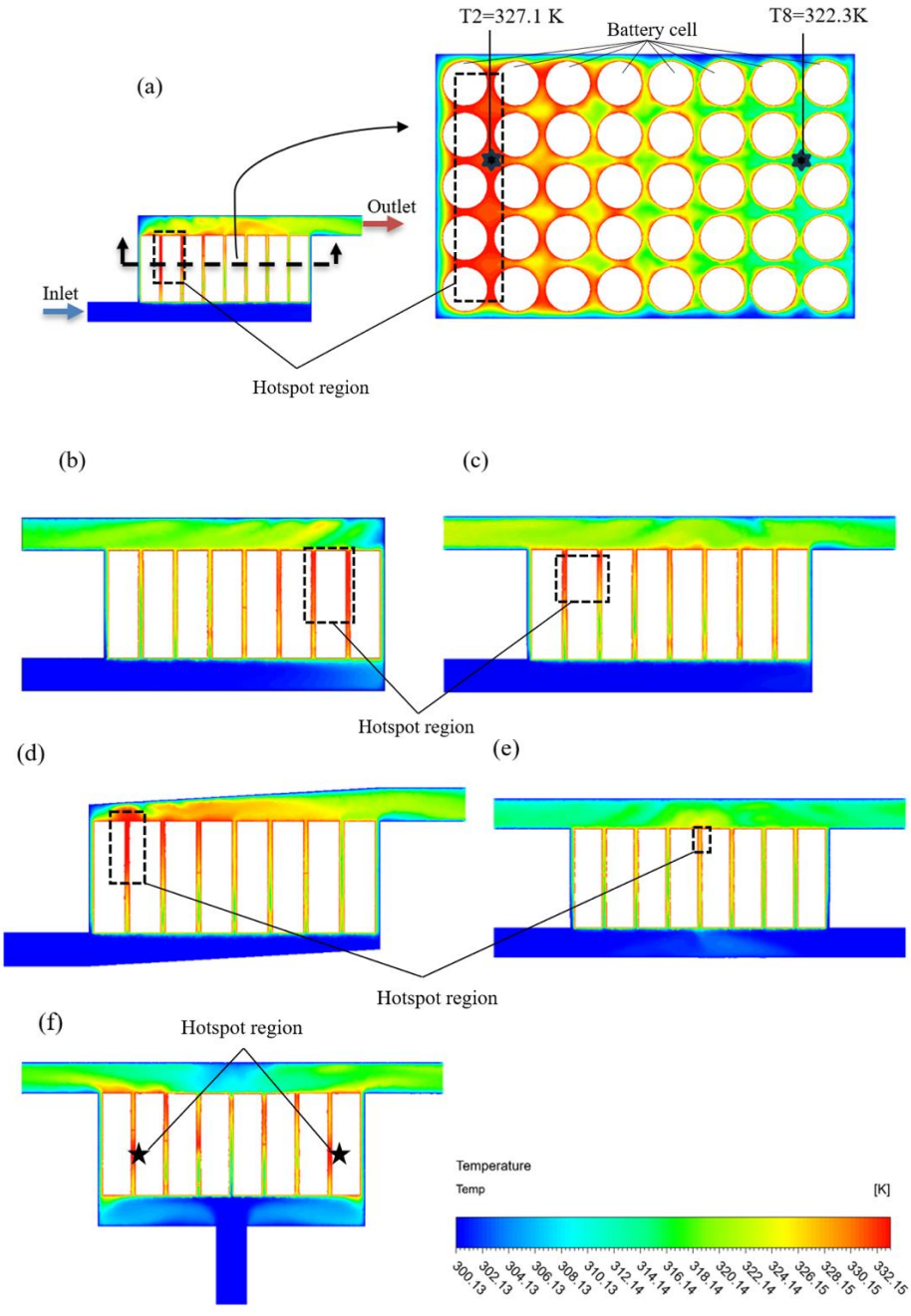

Figure 4. Temperature distribution on the mid-plane of battery geometric enclosures at an inlet velocity of 2 m/s, highlighting hotspot regions and spatial temperature variations for each BTMS configuration: (a) BTMS-Z, (b) BTMS-U, (c) BTMS-J, (d) BTMS-Optimized Z, (e) BTMS-H, and (f) BTMS-T

3.2 Effect of Different Inlet and Outlet Configurations

Figure 4 shows the temperature contour of different enclosure designs. All BTMS designs were simulated with a steady inflow of air-cooling at a room temperature of 300.15 K through the battery with a temperature of 333.15 K. In Figure 4, the temperatures range from 300.13 K (blue) at the inlet to around 332.15 K (red) on the battery walls. As the figure shows, the highest temperature (red) is where the heat is generated from the surface of the battery. The temperature contour plots generally show a lower temperature near the inlet and a higher temperature in the area not far from the outlet [41]. The flow channels in between the batteries show the highest temperature, where the heat from the battery is generated. The results in Figure 5 demonstrate that airflow speeds within the battery pack container vary across different BTMS systems, resulting in significant temperature disparities across the battery cells. In the BTMS-Z enclosure (Figure 4a), we can see that the heat dissipation from the batteries further away from the outlet is worse than from the batteries that are closer to the outlet [47]. The BTMS-J enclosure has a slightly better heat dissipation due to there being two outlets. The optimized BTMS-Z has a slightly better heat dissipation than the normal BTMS-Z, but due to the smaller plenum at the top of the front batteries, the heat dissipation of the front batteries is worse. The BTMS-H has one of the best heat dissipations due to its having two inlets and outlets. The BTMS-T also has good heat dissipation because the inlet is parallel to the cooling channels. This observation underscores the need for careful consideration of enclosure geometry to minimize localized temperature differences.

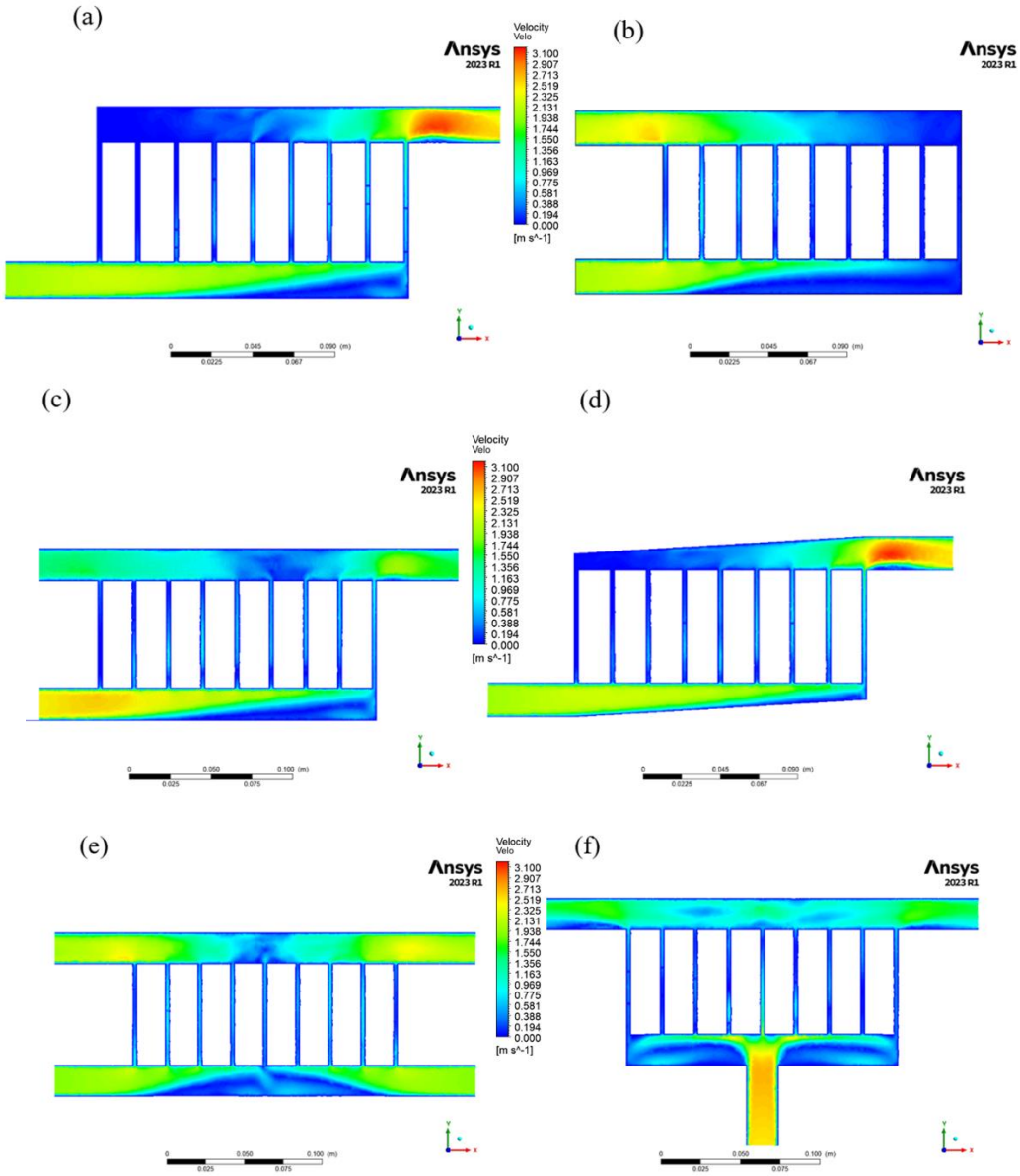

Figure 5. Velocity magnitude contours for various BTMS configurations (a) BTMS-Z, (b) BTMS-U, (c) BTMS-J, (d) BTMS-Optimized Z, (e) BTMS-H, and (f) BTMS-T, showing airflow from the inlet (inlet velocity 2 m/s) to the outlets across the cross-sectional area

Figure 5 shows the velocity contours of the different enclosure designs. Based on the figures shown above, all enclosures were simulated at the battery temperature of 333.15 K. As the figure shows, the BTMS-Z and BTMS-U enclosures have low-velocity zones that are away from the inlet and outlet. This causes some turbulence in that area [48].

The BTMS-J enclosure solves some of these problems by having two outlets. The optimized BTMS-Z also has tapered plenums to help redirect the airflow. The BTMS-H and BTMS-T have the best airflow, which means better heat dissipation. Upon reviewing the velocity contours of all enclosure types, it becomes clear that the primary flow direction is from the inlet to the outlet of the battery enclosure. This unidirectional flow is essential for efficient heat transfer, as fresh air continuously enters the system to dissipate heat generated by the batteries [49] [50]. However, areas showing recirculation, where air circulates within specific regions, may pose challenges, especially near the corners of the battery enclosure. In regions where recirculation occurs, the airflow may stagnate, leading to localized temperature variations and reduced heat dissipation. These recirculation zones can be found in the velocity contours by seeing closed loops or areas with low-velocity magnitudes, as seen in Figure 5 in the BTMS-Z enclosure, which corresponds to the high temperature near the top of the battery. Addressing or optimizing these recirculation zones is critical to ensuring uniform temperature distribution and preventing the formation of hotspots within the battery enclosure [51]. Some limitations are affecting the accuracy of velocity contours, which is due to the simplification of the model geometry.

The observed variation in performance among BTMS designs can be interpreted using fundamental forced convection principles. In this section, Q refers to the total heat transfer rate (W) obtained from CFD post-processing by integrating the surface heat flux over the battery module. This is distinct from the volumetric heat generation term Q in Equation (7) of the Methods section. In forced convection, the rate of heat transfer is proportional to the temperature difference between the battery surface and the surrounding cooling air, as well as the heat transfer coefficient h:

$$Q = hA\left(T_{battery} - T_{air}\right) \tag{8}$$

where A is the battery surface area, T_{battery} is the average battery surface temperature, and T_{air} is the average cooling temperature, rearranging gives:

$$h = \frac{Q}{A\left(T_{battery} - T_{air}\right)} \tag{9}$$

As shown in Figure 6, different BTMS configurations exhibit distinct heat transfer coefficients. BTMS-J achieved the highest coefficient of 190.02 W/m²·K, followed closely by BTMS-H at 187.27 W/m²·K. These designs outperform others, such as BTMS-Z and BTMS-U, which recorded significantly lower values. This variation reflects the influence of enclosure geometry and inlet/outlet configuration on airflow distribution, turbulence generation, and overall thermal performance. One of the key factors contributing to the high heat transfer coefficient in BTMS-J and BTMS-H is the optimized arrangement of inlets and outlets [52], which promotes efficient fluid circulation and heat transfer. Well-positioned inlets ensure that the cooling air reaches critical areas of the battery that require the most heat dissipation. At the same time, the placement of outlets facilitates smooth and effective exhaust of heated air, preventing the formation of stagnation zones where air could accumulate and lose its cooling effectiveness. By maximizing air contact with the battery surface and ensuring steady airflow, BTMS-J and BTMS-H enhance heat dissipation, reflected in their higher heat transfer coefficients. The geometry of the enclosure plays a significant role in directing airflow, impacting both flow velocity and turbulence within the system. Designs like BTMS-J and BTMS-H likely incorporate features that accelerate airflow in key regions (e.g., near hotspots), increasing local convective heat transfer. Moreover, the use of tapered sections or strategically placed baffles may generate beneficial turbulence, which enhances the mixing of air and thus improves heat dissipation. On the other hand, designs like BTMS-Z and BTMS-U with lower heat transfer coefficients may have less optimized flow paths, leading to slower airflow and the potential for laminar flow, which is less effective at transferring heat compared to turbulent flow. These designs might also have more significant thermal boundary layers, where air adjacent to the battery surface moves more slowly, reducing convective heat transfer.

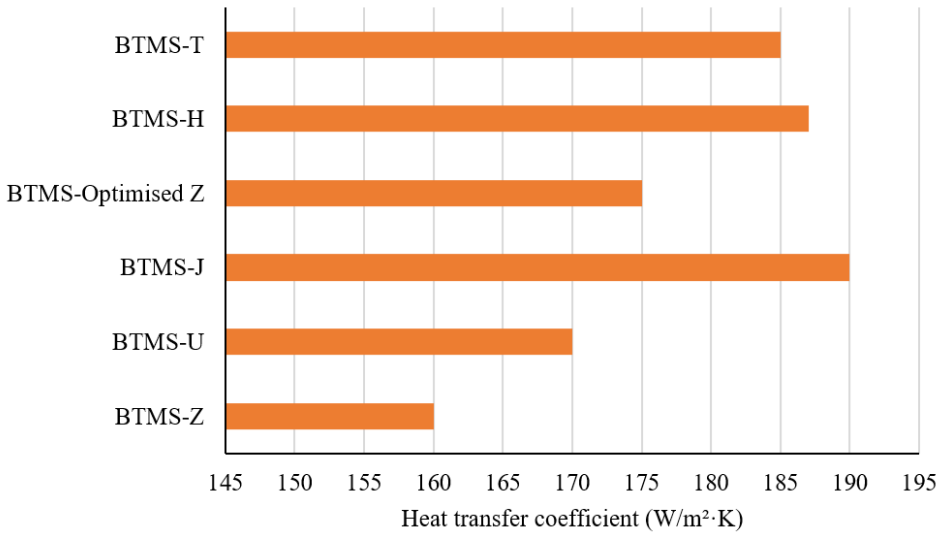

Figure 6. Heat transfer coefficient of all BTMS models

3.3 Effect of Different Inlet Cooling Air Velocity

Analyzing temperature contours from Figure 7, it is evident that heat dissipation is more efficient in the BTMS-Z enclosure at 4 m/s inlet velocity compared to 3 m/s. The temperature distribution patterns indicate improved thermal performance with the higher inlet velocity, showcasing the significance of airflow dynamics in the battery thermal management system. The results depicted in Figure 8 demonstrate the relationship between the average temperature and the inlet velocity for all BTMS models. The data indicate that the highest average temperature, at 317.51 K, is observed at a 2 m/s inlet velocity in BTMS- Optimized Z, while the lowest average temperature, at 307.75 K, is recorded at a 4 m/s inlet velocity. The observed trend shows the impact of inlet velocity on average temperatures within the BTMS. The study of different air inlet velocities has provided valuable insights into their impact on the average temperature within the battery enclosure [52], [53]. A notable observation is the clear correlation between increased inlet velocity and decreased average temperature. The observed decrease in average temperature with increasing inlet velocity is consistent with fundamental convective heat transfer principles [54]. For forced convection, the Nusselt number (Nu)—which is directly proportional to the convective heat transfer coefficient (h)—increases with the Reynolds number (Re) and Prandtl number (Pr) [55], as expressed in empirical correlations of the form $Nu \propto Re^{m}Pr^{n}$. An increase in inlet velocity raises the Reynolds number, thereby increasing Nu and h, which enhances the rate of heat removal from the battery surfaces. This relationship is further amplified by the increased mass flow rate, which reduces the temperature rise of the cooling air as it passes through the enclosure. While higher inlet velocities improve cooling efficiency, they also increase fan power consumption. Moreover, beyond a certain threshold, the incremental reduction in temperature becomes less significant [27], suggesting the existence of an optimal velocity range that balances cooling performance and energy efficiency. Identifying this optimal range is essential for practical BTMS design, where performance gains must be weighed against operational costs and constraints.

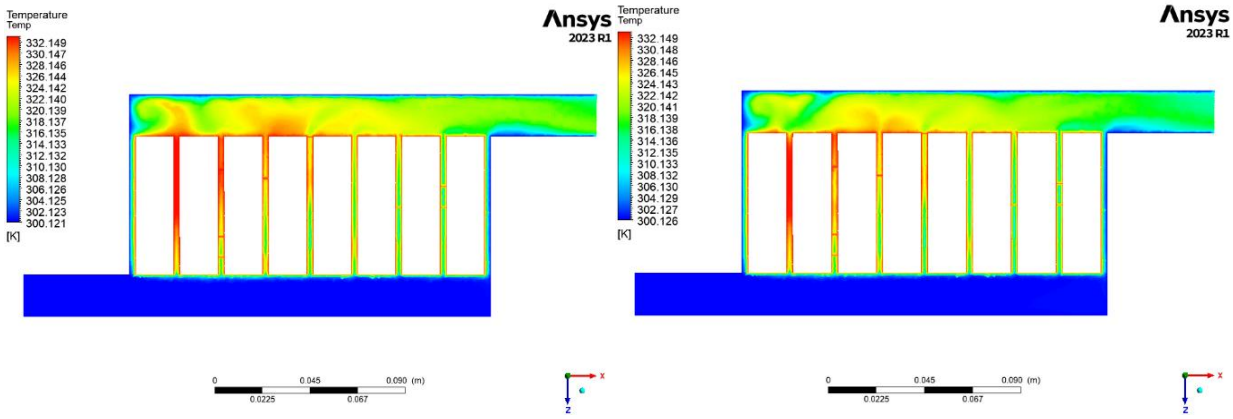

Figure 7. BTMS-Z cross-sectional area of temperature distribution contours at 3 m/s (left) and 4m/s (right) inlet velocity

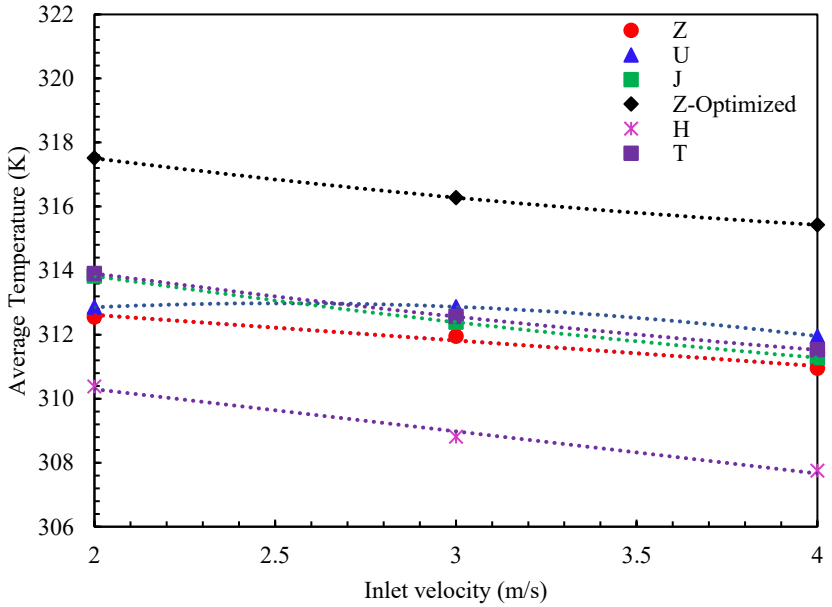

Figure 8. Average temperature in the BTMS according to different air-cooled inlet velocities

3.4 Influence of Inlet and Outlet Sizes

Figure 9 illustrates the relationship between average temperature and inlet/outlet size for the BTMS-Z design at an inlet velocity of 2 m/s. Two inlet/outlet heights—20 mm and 40 mm—were examined to represent realistic dimensional limits for EV battery module cooling ducts. The 20 mm size reflects a compact design often dictated by packaging constraints in space-limited battery enclosures, while the 40 mm size represents a feasible upper bound that can be implemented without significant redesign of the enclosure or vehicle layout [52]. Analysis reveals that the 20 mm inlet/outlet size produced the highest average temperature, 312.54 K (39.39 °C), whereas the 40 mm size resulted in the lowest average temperature, 309.91 K (36.76 °C). Enlarging the inlet and outlet promotes greater airflow exchange, reduces pressure drop, and strengthens convective heat transfer, which collectively support a more uniform temperature distribution and mitigate the occurrence of hotspots. In contrast, smaller openings tend to limit airflow, contributing to localized heating and increased temperature gradients within the battery pack. While this study examined the BTMS-Z design, comparable trends are likely to be observed in other battery thermal management system configurations, with larger inlet/outlet sizes generally associated with lower average enclosure temperatures. Careful consideration of how opening size, airflow resistance, and temperature distribution interact is vital for optimizing system design and balancing thermal management with packaging and manufacturing limitations in electric vehicle applications. Additionally, these findings highlight a key design trade-off: although increased airflow velocity can enhance cooling performance, it also elevates fan power requirements and noise levels. Determining an optimal velocity range for each enclosure type remains an important aspect of system development.

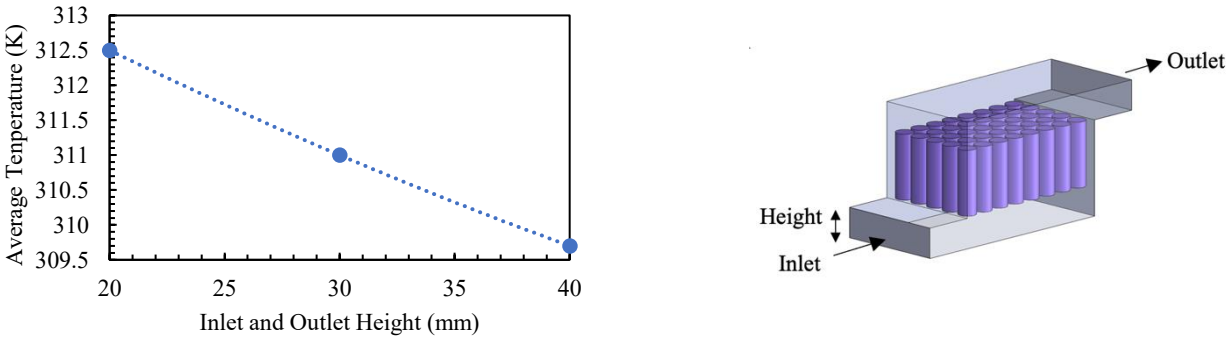

Figure 9. Average temperature according to inlet and outlet size (height)

4. Conclusions

Effective battery thermal management is paramount for enhancing the performance, safety, and service life of electric vehicle batteries. Through detailed computational fluid dynamics simulations, this study investigated how variations in the geometry of the battery thermal management system enclosure, inlet and outlet dimensions, and airflow velocity collectively influence heat dissipation and temperature uniformity. Key findings include:

(i) Superior geometries: BTMS-H and BTMS-J achieved the highest heat transfer coefficients (190.020 W/m²·K and 187.266 W/m²·K, respectively), owing to improved airflow pathways.

(ii) Inlet velocity effect: Increasing the inlet air velocity from 2 m/s to 4 m/s consistently lowered the average enclosure temperature. For BTMS-H, the reduction was from 310.38 K to 307.75 K, highlighting the importance of airflow control.

(iii) Inlet/outlet sizing: Enlarging openings from 20 mm to 40 mm further reduced temperatures, with BTMS-Z dropping from 312.54 K to 309.91 K (36.76 °C), demonstrating the value of optimizing duct dimensions.

These findings offer practical guidance for designing compact, efficient air-cooled battery thermal management systems for electric vehicles. Strategic selection of enclosure geometries that foster uniform airflow distribution, coupled with increasing inlet velocity within operational limits and optimizing duct dimensions, can significantly enhance thermal performance. Such strategies are crucial for preventing localized hotspots, mitigating the risk of thermal runaway, and extending battery lifespan, all vital elements for the safe, reliable, and energy-efficient operation of electric vehicles. The present investigation was conducted under steady-state, idealized conditions, with experimental validation presently restricted to the Z-type configuration. Future research should extend experimental validation to encompass all tested geometries. Furthermore, the modeling approach should incorporate transient simulations to accurately capture dynamic operating behaviors. By addressing these areas, subsequent studies can refine methodologies for battery thermal management systems, thereby facilitating the development of thermally robust, energy-efficient systems that support accelerated electric vehicle adoption. While this study did not explicitly compute electrical efficiency, the observed reductions in peak temperature and improvements in temperature uniformity are well-established factors that lower internal resistance and slow capacity degradation. These thermal enhancements, therefore, represent an indirect yet significant pathway to improving the long-term energy efficiency and lifespan of electric vehicle battery packs. Future studies incorporating coupled electro-thermal modeling are essential to quantitatively determine these efficiency gains.

In conclusion, this work provides clear, evidence-based strategies for enhancing the performance of air-cooled battery thermal management systems through judicious geometry selection, optimized airflow management, and refined inlet and outlet designs. By effectively translating insights gained from computational fluid dynamics into practical engineering

actions, this study bridges the gap between simulation and real-world application, laying a robust foundation for safer, longer-lasting, and more energy-efficient battery systems.

Acknowledgements
The authors would like to thank Universiti Malaysia Pahang Al-Sultan Abdullah for providing the laboratory facilities that enabled this work.

Funding
The authors would like to thank Universiti Malaysia Pahang Al-Sultan Abdullah for providing financial support under RDU230387.

Declaration of Competing Interest
The author declares no conflicts of interest.

CRediT Authorship Contribution Statement
N.H.Johari and H.A.Razak (Conceptualization; Methodology; Formal analysis; Visualisation; Writing – original draft)
M.A.Hamidi and K.Kadirgama (Data curation; Writing - original draft; Resources)

Availability of Data and Materials
The data supporting this study's findings are available on request from the corresponding author.

Ethics Declarations
This study did not involve human participants or animals. Ethical approval was therefore not required.

Generative Artificial Intelligence Declarations
The authors stated that generative AI was not used to generate content, ideas, or theories. We have just utilized AI to enhance readability and refine the language. This was used with extreme human control and oversight. The authors take full responsibility for reviewing and approving the content.

References
[1] K. Obaideen, M.A. Abdelkareem, T. Wilberforce, K. Elsaid, E.T. Sayed, H.M. Maghrabie, et al., "Biogas role in achievement of the sustainable development goals: Evaluation, challenges, and guidelines," *Journal of the Taiwan Institute of Chemical Engineers*, vol. 131, pp. 104207, 2022.
[2] A.G. Olabi, K. Obaideen, K. Elsaid, T. Wilberforce, E.T. Sayed, H.M. Maghrabie, et al., "Assessment of the pre-combustion carbon capture contribution into sustainable development goals SDGs using novel indicators," *Renewable and Sustainable Energy Reviews*, vol. 153, pp. 111710, 2022.
[3] M. Nasiri, H. Hadim, "Advances in battery thermal management: Current landscape and future directions," *Renewable and Sustainable Energy Reviews*, vol. 200, pp. 11461, 2024.
[4] D. Keiner, M. Ram, L.D.S.N.S. Barbosa, D. Bogdanov, C. Breyer, "Cost optimal self-consumption of PV prosumers with stationary batteries, heat pumps, thermal energy storage and electric vehicles across the world up to 2050," *Solar Energy*, vol. 185, pp. 406-423, 2019.
[5] P. Sun, R. Bisschop, H. Niu, X. Huang, "A review of battery fires in electric vehicles," *Fire Technology*, vol. 56, no. 4, pp. 1361–1410, 2020.
[6] F.S. Hwang, T. Confrey, C. Reidy, D. Picovici, D. Callaghan, D. Culliton, et al., "Review of battery thermal management systems in electric vehicles," *Renewable and Sustainable Energy Reviews,* vol. 192, pp. 114171, 2024.
[7] S. Kharabati, S. Saedodin, "A systematic review of thermal management techniques for electric vehicle batteries," *Journal of Energy Storage*, vol. 75, pp. 109586, 2024.
[8] J. Chen, J.E.S. Kang, X. Zhao, H. Zhu, Y. Deng, Q. Peng, Z. Zhang, "Modeling and characterization of the mass transfer and thermal mechanics of the power lithium manganate battery under charging process," *Energy*, vol. 187, pp. 115924, 2019.
[9] M.A. Aziz, A.F. Yusop, M.H. Mat Yasin, M.A. Hamidi, A. Alias, H. Hussin, et al., Study of alcohol fuel of butanol and ethanol effect on the compression ignition (CI) engine performance, combustion and emission characteristic. *IOP Conference Series: Materials Science Engineering*, vol. 257, p. 012079, 2017.
[10] I. Izzudin, A.F. Yusop, S. Sapee, M.A. Hamidi, I.M. Yusri, R. Mamat, et al. Experimental studies of single cylinder engine run on diesel-biodiesel-butanol blends. *IOP Conference Series: Materials Science Engineering*, vol. 863, p. 012060, 2020.
[11] S. Daud, M.A. Hamidi, R. Mamat, D.M. Nafiz, A Prediction of graphene nanoplatelets addition effects on diesel engine emissions. *International Journal of Automotive and Mechanical Engineering*, vol. 20, no. 3, pp. 10758–10766, 2023.
[12] S. Daud, M.A. Hamidi, R. Mamat, R. Design of experiment to predict the effects of graphene nanoplatelets addition to diesel engine performance. *Automotive Experiences*, vol. 5, no. 3, pp. 467–476, 2022.

[13] M. Junginger, A. Louwen, "Technological learning in the transition to a low-carbon energy system: Conceptual issues, empirical findings, and use," in *Energy Modeling*, Academic Press, pp. 145-163, 2020.
[14] M.A. Abdelkareem, H.M. Maghrabie, A.G. Abo-Khalil, O.H.. Adhari, E.T. Sayed, A. Radwan, et al., "Battery thermal management systems based on nanofluids for electric vehicles," *Journal of Energy Storage*, vol. 50, pp. 104385, 2022.
[15] S.K. Mohammadian, Y. Zhang, "Thermal management optimization of an air-cooled Li-ion battery module using pin-fin heat sinks for hybrid electric vehicles," *Journal of Power Sources*, vol. 273, pp. 431-439, 2015.
[16] T. Wang, K.J. Tseng, J. Zhao, Z. Wei, "Thermal investigation of lithium-ion battery module with different cell arrangement structures and forced air-cooling strategies," *Applied Energy*, vol. 134, pp. 229-238, 2014.
[17] M. Akbarzadeh, T. Kalogiannis, J. Jaguemont, L. Jin, H. Behi, D. Karimi, et al., "A comparative study between air cooling and liquid cooling thermal management systems for a high-energy lithium-ion battery module," *Applied Thermal Engineering*, vol. 198, pp. 117503, 2021.
[18] Y. Chen, K. Chen, Y. Dong, X. Wu, "Bidirectional symmetrical parallel mini-channel cold plate for energy efficient cooling of large battery packs," *Energy*, vol. 242, pp. 122553, 2022.
[19] F. Samimi, A. Babapoor, M. Azizi, G. Karimi, "Thermal management analysis of a Li-ion battery cell using phase change material loaded with carbon fibers," *Energy*, vol. 96, pp. 355-371, 2016.
[20] X. Zhang, G. Su, J. Lin, A. Liu, C. Wang, Y. Zhuang, "Three-dimensional numerical investigation on melting performance of phase change material composited with copper foam in local thermal non-equilibrium containing an internal heater," *International Journal of Heat and Mass Transfer*, vol. 170, pp. 121021, 2021.
[21] J. Liang, Y. Gan, Y. Li, "Investigation on the thermal performance of a battery thermal management system using heat pipe under different ambient temperatures," *Energy Conversion and Management*, vol. 155, pp. 1-9, 2018.
[22] J. Zhao, P. Lv, Z. Rao, "Experimental study on the thermal management performance of phase change material coupled with heat pipe for cylindrical power battery pack," *Experimental Thermal and Fluid Science*, vol. 82, pp. 182-188, 2017.
[23] C. Yang, H. Xi, M. Wang, "Structure optimization of air cooling battery thermal management system based on lithium-ion battery," *Journal of Energy Storage*, vol. 59, pp. 106538, 2023.
[24] K. Chen, Z. Zhang, B. Wu, M. Song, X. Wu, "An air-cooled system with a control strategy for efficient battery thermal management," *Applied Thermal Engineering*, vol. 236, pp. 121578, 2024.
[25] X. Zhang, J. Yao, L. Zhu, J. Wu, D. Wei, Q. Wang, et al., "Experimental and simulation investigation of thermal runaway propagation in lithium-ion battery pack systems," *Journal of Energy Storage*, vol. 77, pp. 109868, 2024.
[26] A. Rahmani, M. Dibaj, M. Akrami, "Recent Advancements in Battery Thermal Management Systems for Enhanced Performance of Li-Ion Batteries: A Comprehensive Review," *Batteries*, vol. 10, no. 8., pp. 265, 2024.
[27] G. Zhang, W. Shen, X. Wei, "Lithium-ion battery thermal safety evolution during high-temperature nonlinear aging," *Fuel*, vol. 362, pp. 130845, 2024.
[28] G. Zhang, X. Wei, S. Chen, G. Wei, J. Zhu, X. Wang, et al., "Research on the impact of high-temperature aging on the thermal safety of lithium-ion batteries," *Journal of Energy Chemistry*, vol. 87, pp. 378-389, 2023.
[29] S. Yang, J. Lin, Z. Zhang, C. Zhang, X. Zheng, W. Xie, et al., "Advanced engineering materials for enhancing thermal management and thermal safety of lithium-ion batteries: A review," *Frontiers in Energy Research*, vol. 10, pp. 949760, 2022.
[30] S. Pan, C. Ji, S. Wang, B. Wang, "Study on the performance of parallel air-cooled structure and optimized design for lithium-ion battery module," *Fire Technology*, vol. 56, pp. 2623-2647, 2020.
[31] X. Lan, X. Li, S. Ji, C. Gao, Z. He, "Design and optimization of a novel reverse layered air-cooling battery management system using U and Z type flow patterns," *International Journal of Energy Research*, vol. 46, pp. 14206-14226, 2022.
[32] J. Zhang, X. Wu, K. Chen, D. Zhou, M. Song, "Experimental and numerical studies on an efficient transient heat transfer model for air-cooled battery thermal management systems," *Journal of Power Sources*, vol. 490, pp. 229539, 2021.
[33] S.B. Zhang, X. He, N.C. Long, Y.J. Shen, Q. Gao, "Improving the air-cooling performance for lithium-ion battery packs by changing the air flow pattern," *Applied Thermal Engineering*, vol. 221, pp. 119825, 2023.
[34] F. He, H. Wang, L. Ma, "Experimental demonstration of active thermal control of a battery module consisting of multiple Li-ion cells," *International Journal of Heat and Mass Transfer*, vol. 91, pp. 630-639, 2015.
[35] S. Wang, K. Li, Y. Tian, J. Wang, Y. Wu, S. Ji, "Improved thermal performance of a large laminated lithium-ion power battery by reciprocating air flow," *Applied Thermal Engineering*, vol. 152, pp. 445-454, 2019.
[36] Y. Liu, J. Zhang, "Self-adapting J-type air-based battery thermal management system via model predictive control," *Applied Energy*, vol. 263, pp. 114640, 2020.
[37] R.B. Langtry, F.R. Menter, "Correlation-based transition modeling for unstructured parallelized computational fluid dynamics codes," *AIAA Journal*, vol. 47, pp. 2894-2906, 2009.
[38] R.B. Langtry, F.R. Menter, S.R. Likki, Y.B. Suzen, P.G. Huang, S. Völker, "A correlation-based transition model using local variables - Part II: Test cases and industrial applications," *Journal of Turbomachinery*, vol. 128, pp. 423-434, 2006.
[39] N.H. Johari, C. Menichini, M. Hamady, X.Y. Xu, "Computational modeling of low-density lipoprotein accumulation at the carotid artery bifurcation after stenting," *International Journal for Numerical Methods in Biomedical Engineering,* vol. 39, no. 12, pp. e3772, 2023.

[40] N.H. Johari, M. Hamady, X.Y. Xu, "A computational study of the effect of stent design on local hemodynamic factors at the carotid artery bifurcation," *Artery Research*, vol. 26, pp. 161-169, 2020.
[41] K. Chen, W. Wu, F. Yuan, L. Chen, S. Wang, "Cooling efficiency improvement of air-cooled battery thermal management system through designing the flow pattern," *Energy*, vol. 167, pp. 781-790, 2019.
[42] M. Falcone, E.P.B. De Volo, A. Hellany, C. Rossi, B. Pulvirenti, "Lithium-ion battery thermal management systems: A survey and new CFD results," *Batteries*, vol. 7, pp. 1-20, 2021.
[43] D.K. Sharma, A. Prabhakar, "A review on air cooled and air centric hybrid thermal management techniques for Li-ion battery packs in electric vehicles," *Journal of Energy Storage*, vol. 41, pp. 102885, 2021.
[44] J. Zhang, X. Wu, D. Zhou, Q. Li, X. Li, K. Chen, "Experimental and numerical investigation on efficient optimization of battery thermal management systems," *Applied Thermal Engineering*, vol. 221, pp. 119821, 2023.
[45] K. Chen, M. Song, W. Wei, S. Wang, "Structure optimization of parallel air-cooled battery thermal management system with U-type flow for cooling efficiency improvement," *Energy*, vol. 145, pp. 603-613, 2018.
[46] Y. Zhang, X. Song, C. Ma, D. Hao, Y. Chen, "Effects of the structure arrangement and spacing on the thermal characteristics of Li-ion battery pack at various discharge rates," *Applied Thermal Engineering*, vol. 165, pp. 114610, 2020.
[47] X. Peng, C. Ma, A. Garg, N. Bao, X. Liao, "Thermal performance investigation of an air-cooled lithium-ion battery pack considering the inconsistency of battery cells," *Applied Thermal Engineering*, vol. 153, pp. 596-603, 2019.
[48] H.A. Hasan, H. Togun, A.M. Abed, N. Biswas, H.I. Mohammed, "Thermal performance assessment for an array of cylindrical Lithium-Ion battery cells using an Air-Cooling system," *Appl Energy*, vol. 346, pp. 121354, 2023.
[49] C. Wang, H. Xi, M. Wang, "Investigation on forced air-cooling strategy of battery thermal management system considering the inconsistency of battery cells," *Applied Thermal Engineering*, vol. 214, pp. 118841, 2022.
[50] B. Gogoi, H. Deka, B. Bora, et al., "Optimizing thermal performance in air-cooled Li-ion battery packs with vortex generators for cleaner energy storage," *Scientific Reports*, vol. 15, 25477, 2025.
[51] L. Wang, Y. Tang, J. Yu, W. Qin, Y. Zhang, G. Wang, et. al., "Bound optimization by quadratic approximation for heat-dissipation-oriented design of an air-cooled lithium battery energy storage cabinet," *Symmetry*, vol. 18, pp. 107, 2026.
[52] J. Mustafa, "Numerical investigation of the effect of inlet dimensions air duct and distance of battery packs for thermal management of three lithium-ion battery packs," *Journal of Energy Storage*, vol. 48, pp. 103959, 2022.
[53] B. Yazhini, S. Ramabalan, Ramalingam Senthil, "Experimental study of forced-air cooling with heat spreaders for lithium-ion battery thermal management," *Case Studies in Thermal Engineering*, vo. 76, pp. 107347, 2025.
[54] F. Vaz, J.V. Silva, V. Monteiro, F.P. Brito, "CFD-driven design of an air-cooling system for lithium-ion battery packs in a formula student car," *Energies*, vol. 18, pp. 5436, 2025.
[55] Q. Chen, M. Wang, N. Pan, Z.Y. Guo, "Optimization principles for convective heat transfer," *Energy*, vol. 34, pp. 1199-1206, 2009.

Nomenclature

Symbol/ Abbreviation	Description
A	Battery surface area
α	Dissipation rate
BTMS	Battery Thermal Management System
CFD	Computational Fluid Dynamics
EV	Electric Vehicle
F_1	Blending Function (in SST-Tran model)
h	Heat transfer coefficient
HEV	Hybrid Electric Vehicle
ICE	Internal Combustion Engine
k	Turbulent Kinetic Energy (in turbulence model) / Thermal Conductivity (in heat transfer)
μ	Dynamic Viscosity
μ_t	Turbulent Viscosity
N_u	Nusselt number
PHEV	Plug-in Hybrid Electric Vehicle
p	Pressure
P_k	Turbulence Production Term
PCMs	Phase Change Materials
Pr	Prandtl number
Q	Heat Generated by the Battery Cells
RANS	Reynolds-Averaged Navier-Stokes Equations

Re	Reynolds number
ρ	Density
σ_a, σ_k, σ_γ, σ_ω	Model Constants for Turbulent Equations
SST-Tran	Shear Stress Transport with Transitional Model
T	Temperature
u_i, u_j	Velocity Components in i and j directions
W	Heat transfer rate
ω	Specific Rate of Dissipation

.